PAPER

Kinetics control over the Schiff base formation reaction for fabrication of hierarchical porous carbon materials with tunable morphology for high-performance supercapacitors

To cite this article: Ling Liu *et al* 2021 *Nanotechnology* **32** 305602

IOP Publishing Nanotechnology
Nanotechnology 32 (2021) 305602 (11pp) https://doi.org/10.1088/1361-6528/abf59d

Kinetics control over the Schiff base formation reaction for fabrication of hierarchical porous carbon materials with tunable morphology for high-performance supercapacitors

Ling Liu[1], Yuntong Li[1], Zhenwu Lu[1], Ting Chen[1], Qipeng Cai[1], Yiting Xu[1], Birong Zeng[1], Conghui Yuan[1,*], Shiao-Wei Kuo[2] and Lizong Dai[1,*]

[1] Fujian Provincial Key Laboratory of Fire Retardant Materials, College of Materials, Xiamen University, Xiamen, 361005, People's Republic of China
[2] Department of Materials and Optoelectronic Science, Center for Nanoscience and Nanotechnology, National Sun Yat-Sen University, Kaohsiung 804, Taiwan

E-mail: yuanch@xmu.edu.cn and lzdai@xmu.edu.cn

Received 2 February 2021, revised 28 March 2021
Accepted for publication 6 April 2021
Published 4 May 2021

Abstract

Schiff base formation reaction is highly dynamic, and the microstructure of Schiff base polymers is greatly affected by reaction kinetics. Herein, a series of Schiff base cross-linked polymers (SPs) with different morphologies are synthesized through adjusting the species and amount of catalysts. Nitrogen/oxygen co-doped hierarchical porous carbon nanoparticles (HPCNs), with tunable morphology, specific surface area (SSA) and porosity, are obtained after one-step carbonization. The optimal sample (HPCN-3) possesses a coral reef-like microstructure, high SSA up to 1003 $m^2\ g^{-1}$, and a hierarchical porous structure, exhibiting a remarkable specific capacitance of 359.5 $F\ g^{-1}$ (at 0.5 $A\ g^{-1}$), outstanding rate capability and cycle stability in a 1 M H_2SO_4 electrolyte. Additionally, the normalized electric double layer capacitance (EDLC) and faradaic capacitance of HPCN-3 are 0.239 $F\ m^{-2}$ and 10.24 $F\ g^{-1}$ respectively, certifying its superior electrochemical performance deriving from coral reef-like structure, high external surface area and efficient utilization of heteroatoms. The semi-solid-state symmetrical supercapacitor based on HPCN-3 delivers a capacitance of 55 $F\ g^{-1}$ at 0.5 $A\ g^{-1}$, good cycle stability of 86.7% after 5000 GCD cycles at 10 $A\ g^{-1}$, and the energy density ranges from 7.64 to 4.86 $Wh\ kg^{-1}$.

Supplementary material for this article is available online

Keywords: kinetics control, Schiff base, carbon materials, hierarchical porous structure, tunable morphology, semi-solid-state supercapacitor

(Some figures may appear in colour only in the online journal)

1. Introduction

As the global energy crisis is aggravating, the demand for sustainable, clean and environmentally harmonious energy storage equipment becomes imminent. Supercapacitors,

* Authors to whom any correspondence should be addressed.

newly developed energy storage devices, possess many merits, complementing secondary batteries, such as extra-high-power density, instant charge/discharge ability and superb durability [1–3]. The commercial value of supercapacitors, to a large extent, depends on the supercapacitive performance of electrode materials. Therefore, three categories of electrode materials, including transition metal oxides/sulfides [4–6], conductive polymers [7, 8] and carbon materials [1, 9, 10], have been developed. Among them, heteroatom-doped carbon materials have attracted substantial attention for their high specific surface area (SSA), excellent chemical stability, terrific electrical conductivity and adjustable heteroatom content.

To date, heteroatom-doped carbon materials with large SSAs, different morphologies, pore structures and compositions have been designed and fabricated, and the effects of SSA, porosity and composition on the supercapacitive performance has been investigated [11–16]. Importantly, the morphology of the carbon materials may not only affect the available utilization of SSA, but also influence the ion diffusion rate during the redox reaction [17–20]. Thus, a comparative investigation of the relationship between the morphology of electrode materials and their corresponding capacitive performance is of great significance for designing high-performance electrode materials in supercapacitors.

Fabrication of high-performance carbon materials via elegantly designed polymeric precursors has developed into a generally adopted tactic, which not only can be used to adjust the morphology and pore structure of the carbon materials easily, but also introduce different heteroatoms into the carbon matrix [11, 12, 16, 21, 22]. The Schiff base formation reaction is beneficial for the generation of rigid cross-linked polymer networks, thus being superior for the design of carbon materials, with high capacitance and energy density [23–26]. For example, Zhu *et al* synthesized nitrogen-rich microporous carbon spheres (N-MCSs) through a simple Schiff base reaction followed with a one-step carbonization-activation procedure, which displayed a high capacitance of 292 F g^{-1} at a current density of 1.0 A g^{-1} and outstanding cycling stability [11]. Li *et al* synthesized nitrogen-doped hierarchical porous carbon materials (Ta-NCas) on the basis of the Schiff base formation reaction, and Ta-NCas exhibited remarkable supercapacitive performance in acidic (1 M H_2SO_4) and alkaline (6 M KOH) electrolytes simultaneously [12].

Although there have been tremendous advances in the design of Schiff base polymers for high-performance carbon materials, few examples have paid attention to the morphology control of Schiff base polymer precursors through the adjustment catalyst. Herein, setting from rigid monomers of 1, 3, 5-tris(4-aminophenyl)benzene (TAB) and 1, 4-terephthalaldehyde (TPA), we prepared a series of cross-linked Schiff base polymers (denoted as SPs) using acidic catalysts. The morphology and size of the resultant SPs can be easily adjusted by the catalyst species and concentration. After a simple pyrolysis procedure, nitrogen/oxygen co-doped hierarchical porous carbon nanoparticles (denoted as HPCNs) with different morphologies can be obtained. HPCNs exhibit superior supercapacitive performance, and the optimal sample (HPCN-3) has a capacitance of 359.5 F g^{-1} in a 1 M H_2SO_4 electrolyte at 0.5 A g^{-1}. A semi-solid-state symmetrical supercapacitor based on HPCN-3 electrode demonstrates a capacitance of 55 F g^{-1} (at 0.5 A g^{-1}). We pay particular attention to the effects of morphology, SSA and pore structure on the electric double layer capacitance (EDLC), pseudo-capacitance and the overall specific capacitance of the carbon materials.

2. Experimental section

2.1. Materials

TAB and trifluoromethanesulfonic acid (CF_3SO_3H, TfOH) were supplied by J&K Company. TPA, polyvinylidene fluoride (PVDF), N-methylpyrrolidone (NMP) and polyvinyl alcohol (PVA) were purchased from Aladdin Company. Acetic acid (CH_3COOH, HAc), sulfuric acid (H_2SO_4, SA), mesitylene, 1, 4-dioxane and ethanol were obtained from Shanghai Chemical Reagent Industry. All chemicals were used as received without further purification.

2.2. Preparation of HPCNs

In a typical synthetic procedure, TAB (0.703 g, 2.0 mmol) and TPA (0.40 g, 3.0 mmol) were placed in a round-bottom flask, and dissolved in 5 ml of a mixed solvent containing mesitylene and 1, 4-dioxane (v: v = 1: 4). Subsequently, the catalyst (such as TfOH, SA and HAc) was introduced into the reaction solution under vigorous stirring. After 10 min reaction, precipitates were obtained by filtration followed with washing with ethanol three times. Orange solid powders of SPs were obtained. These powders were placed in a muffle furnace and carbonized for 2 h with a heating rate of 5 °C min^{-1} in an Ar atmosphere to afford HPCNs.

As displayed in table 1, distinguished from the concentration of catalyst TfOH and the carbonization temperature, the carbon materials are named HPCN-1, HPCN-2, HPCN-3, HPCN-6 and HPCN-7, respectively. Also, SP-4 and SP-5 were prepared by using SA and HAc as catalysts, respectively.

2.3. Characterization

Fourier-transform infrared (FT-IR) spectra were recorded on a Nicolet iS10 equipped with an ATR cell. Scanning electron microscopy (SEM) images were taken from an SU-70 instrument under an acceleration voltage of 10 kV. Transmission electron microscopy (TEM) images were obtained from a JEM2100 instrument with an acceleration voltage of 200 kV. The high-angle annular dark-field scanning transmission electron microscopy (HAADF-STEM) images and elemental energy-dispersive x-ray spectroscopy (EDS) mapping were characterized by a FEI Talos F200 microscope operated at 300 kV. Raman spectra were tested on an Xplora with an excitation wavelength of 638 nm. X-ray photoelectron spectroscopy (XPS) measurement was carried out on a PHI

Table 1. Sample details of SPs and HPCNs.

SPs	Catalyst				
	Name	Amount/μl	c_H^+/mol l^{-1}	Temperature/°C	HPCN
SP-1	TfOH	5	0.0112	850	HPCN-1
SP-2		15	0.0339		HPCN-2
SP-3		25	0.0565		HPCN-3
SP-4	SA	25	0.1878		HPCN-4
SP-5	HAc	200	0.7		HPCN-5
SP-3	TfOH	25	0.0565	750	HPCN-6
				950	HPCN-7

Quantum-2000 photoelectron spectrometer (Al Kα with 1486.6 eV) and all the spectra were calibrated with the C 1 s peak at 284.8 eV as an internal standard. Nitrogen sorption isotherms were investigated by an ASAP 2460 system, and all samples were degassed at 120 °C for 24 h in a vacuum before measurements.

2.4. Electrochemical measurement

All electrochemical tests were carried out on a CHI 760E electrochemical station using a 1 M H_2SO_4 electrolyte at room temperature.

In a standard three-electrode system, HPCNs were used as the working electrodes. Typically, 5 mg active materials (95 wt%) and PVDF (5 wt%) were mixed in 63 μl of NMP to form a uniform slurry. Then 2 μl slurry was dropped onto a glassy carbon electrode (diameter: 3 mm), which was polished smoothly using different sizes of Al_2O_3 powders. Finally, the electrode was dried at 80 °C under vacuum for 12 h. The mass loading of active materials on each working electrode was 0.15 mg. Saturated calomel electrode (SCE), platinum foil were served as reference electrode and counter electrode, respectively. Cyclic voltammetry (CV), gravimetric charge/discharge (GCD) and electrochemical impedance spectroscopy (EIS) tests were performed with a voltage window of 0–1 V. The calculation formula (equation (1)) for the specific capacitance is shown in the Supplementary Information.

Also, a semi-solid-state symmetrical supercapacitor was constructed by sandwiching a PVA/H_2SO_4 gel electrolyte (size: 1 cm × 1 cm × 1 mm) between two pieces of HPCN-3 electrodes (the coating area is 1 cm × 1 cm), and carbon film served as the current collector. To be specific, the as-prepared HPCN-3 slurry was evenly coated on the carbon film cleaned with ethanol to obtained an electrode layer, followed by drying at 80 °C for 12 h. The mass loading of active materials on each electrode layer was 1.5 mg cm^{-2}. PVA/H_2SO_4 gel was prepared using the following procedure: 6 g PVA was dissolved into 30 ml of 1 M H_2SO_4 aqueous solution at 95 °C to make the solution completely clear. All measurements were carried out with a potential window of 0–1 V. Equations (2)–(6), for the specific capacitance obtained from GCD curves, energy density, and power density, are given in the Supplementary Information.

3. Results and discussion

The Schiff base formation reaction has been extensively employed to generate various functional polymer materials such as stimuli–response nanoparticles [27, 28], smart hydrogels [29, 30], covalent organic frameworks (COFs) [31, 32], and so on. Since this reaction is highly dynamic, the structure of the Schiff base polymer networks is greatly affected by the reaction kinetics. In this work, we use TAB and TPA as monomers and different amounts or types of acids including TfOH, SA and HAc as catalysts to create a series of SPs. As illustrated in figure 1, these reactions are easily carried out in a mixed solvent of mesitylene and 1, 4-dioxane (v: v = 1: 4) in the presence of the catalysts. Notably, the morphology of the SPs can be easily adjusted by changing the concentration or species of the acidic catalysts. After a simple pyrolysis procedure, HPCNs with different morphologies can be constructed.

3.1. Morphology and structure of the polymer precursors and carbon materials

Figure S1 (available online at stacks.iop.org/NANO/32/305602/mmedia) gives the FT-IR spectra of the monomers and SPs. Apart from the difference in signal intensity of unreacted –NH_2 and –CHO groups, SP-3, SP-4 and SP-5 show similar FT-IR spectra. Compared with the FT-IR spectra of monomers, the peaks at 3353 (the stretching vibration of -NH_2 groups) and 1685 cm^{-1} (the stretching vibration of C=O bond) of SPs attenuate substantially.

A new characteristic absorption peak at 1621 cm^{-1} ascribed to the stretching vibration of C=N bond appears in the FT-IR spectra of SPs [11, 12, 31, 33]. These results provide an indication for the cross-linking reaction between TAB and TPA.

The composition and morphology of SPs were characterized to clarify the effect of the catalysts on the cross-linking reaction. Table S1 displays the element contents of SPs calculated from XPS spectra. N content changes slightly with the altering of the acidic catalyst concentration or species, which may be caused by the different condensation polymerization degrees between TAB and TPA. To give an insight into the effect of catalysts on the Schiff base reaction, N 1 s XPS spectra of TAB monomer and SPs were analyzed (figure S2 and table S2). For TAB, only one peak centered at

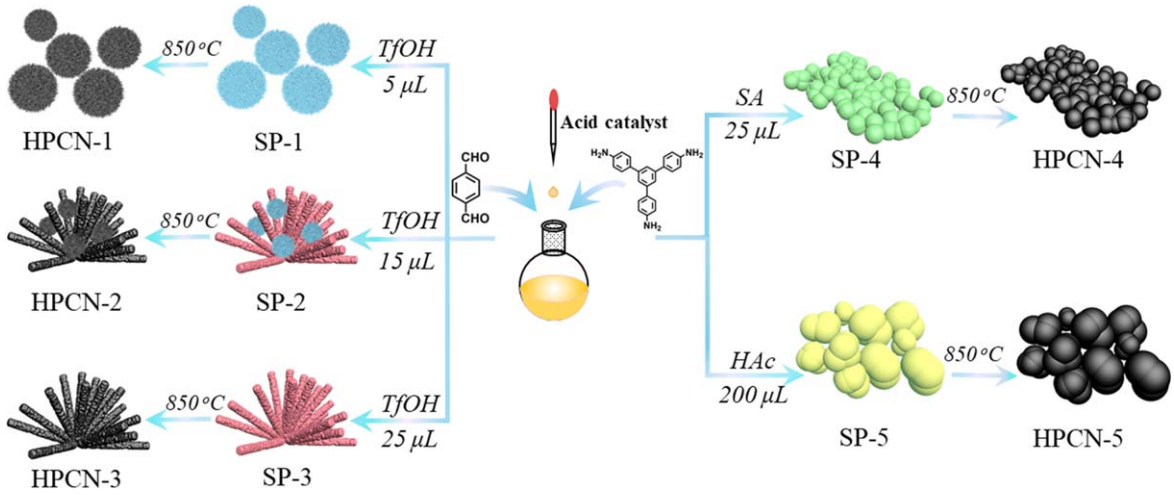

Figure 1. Synthetic process of SPs and HPCNs.

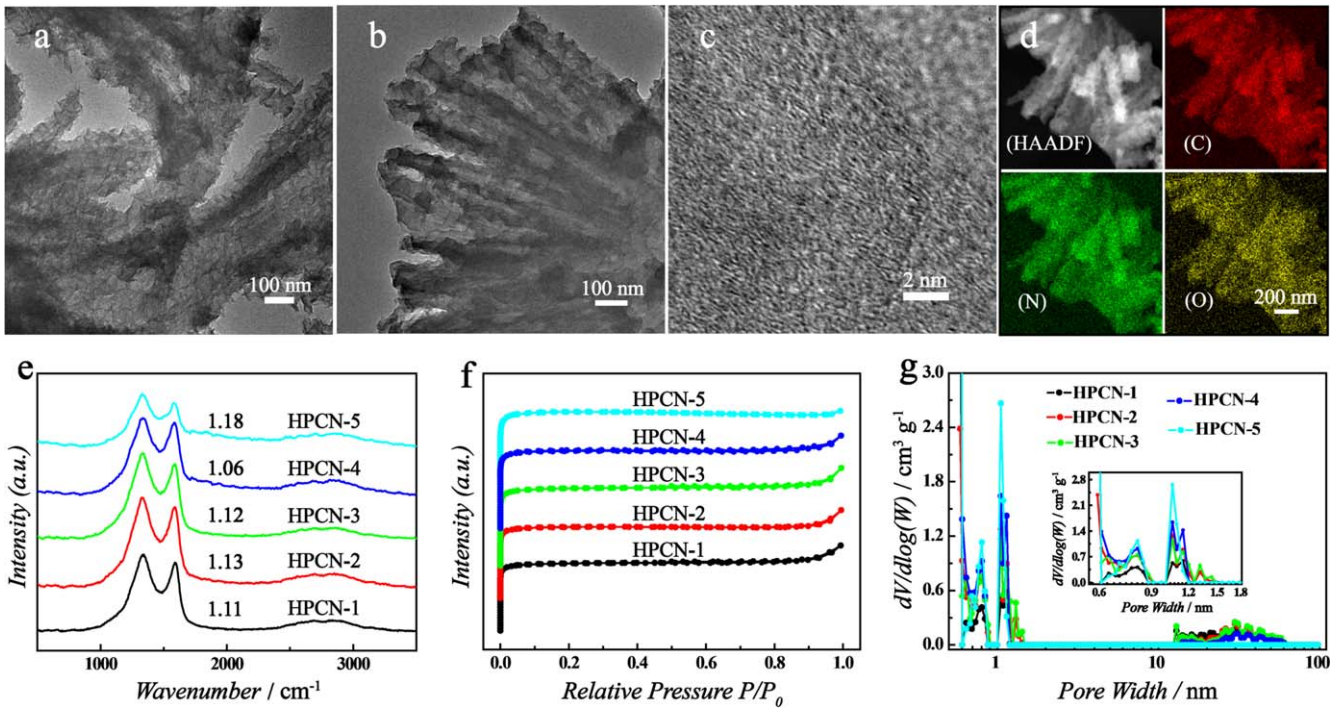

Figure 2. TEM images of SP-3 (a) and HPCN-3 (b), (c), HAADF-STEM image and EDS element mapping for HPCN-3 (d), Raman spectra (e), N_2 adsorption/desorption isotherms (f) and the NLDFT pore size distribution (g) of HPCNs.

399.6 ± 0.1 eV is observed, ascribed to the NH_2 group. For SPs, three new peaks appear, C=N (398.9 ± 0.1 eV), –C=NH^+ (401.2 ± 0.1 eV) and -NH_3^+ (401.9 ± 0.1 eV), except for the NH_2 peak (399.6 ± 0.1 eV) with evidently decreased intensity, certifying the successful synthesis of cross-linked polymers and the uncompleted Schiff base reaction [34–36]. Intriguingly, apart from SP-5, with the increase of the concentration of acidic catalyst, the -NH_2 content gradually decreases and the contents of generated C=N, –C=NH^+ and –NH_3^+ simultaneously increase. These results imply that strong acidic catalyst can promote the Schiff base reaction and the excessive H^+ induces the protonation of the imine bond and amino group simultaneously. Figures 2(a), S3, and S4 show the SEM and TEM images of SPs. SP-1, prepared using 5 μl of TfOH as the catalyst, exhibits a surface-wrinkled spherical structure with an average diameter of approximately 400 nm. SP-3, catalyzed with 25 μl of TfOH, displays a coral reef-like shape, while SP-2, catalyzed with 15 μl of TfOH, shows both spherical and coral reef-like shapes. These results illustrate that changing the concentration of TfOH can adjust the morphology of the precursors because of the variation of reaction rates. SP-4 using 25 μl of SA and SP-5 using 200 μl of HAc as catalysts both display adhesively spheroidal structures, but the particle size of SP-5 is much larger than that of SP-4. The appearance of adhesively spheroidal morphology may be because the density of the active center is too high, resulting from the high concentration of acidic catalyst; therefore the products are

easy to aggregate. To a certain extent, acidic catalysts with stronger acidity or higher concentration can accelerate the imine bond formation reaction rate [37]. We infer that a high reaction rate leads to the formation of reef-like Schiff base polymer precursors, while a low reaction rate results in the formation of spherical Schiff base polymer precursors.

HPCNs can preserve the original morphologies of their corresponding precursors after carbonization (figures 2(b) and S5). High-resolution TEM images of the carbon materials (figures 2(c) and S6) show an apparently porous structure. Evident lattice fringes can be identified in the carbon materials except HPCN-5, suggesting that smaller particle size is helpful for the formation of ordered structures. EDS element mapping of HPCN-3 shown in figure 2(d) confirms that the coexistence of C, N, and O elements and each element is evenly dispersed in the carbon matrix. This is beneficial for enhancing the utilization of heteroatoms and improving the surface wettability of electrode materials, as well as enlarging the faradaic capacitance produced by nitrogen- and oxygen-containing functional groups [1, 9, 12, 15, 38, 39].

The Raman spectra are acquired to characterize the carbon structures (figure 2(e)). All carbon materials display two typical peaks located at 1341 cm^{-1} (D bond, symbol of disordered structure and defects) and 1589 cm^{-1} (G bond, related to ordered graphitized structure), respectively. The intensity ratio of the D and G bands (I_D/I_G) is used to assess the degree of graphitization [38, 40, 41]. The I_D/I_G values of HPCN-1, HPCN-2 and HPCN-3 are 1.11, 1.13 and 1.12, respectively, implying that the TfOH concentration can not remarkably affect the graphitization degree. For HPCN-4, the I_D/I_G value (1.06) is clearly lower. This may be due to the smaller particle size, which is conducive to the formation of ordered structures during carbonization. Conversely, the I_D/I_G value of HPCN-5 (1.18) is evidently higher, which can be attributed to the larger content of heteroatoms as certificated by the XPS results [14, 42].

Nitrogen adsorption–desorption measurements at 77 K were performed to analyze the SSA and pore properties of HPCNs. As displayed in figures 2(f) and S7, all the samples exhibit fast nitrogen uptake under relatively low pressure ($P/P_0 < 0.01$), indicating the presence of abundant micropores (<2 nm), which is valuable to increase the SSA and provide a sufficient electrode/electrolyte contact interface for ion or charge accumulation [39, 43, 44]. Except HPCN-5, samples show a narrow hysteresis loop ($0.4 \leqslant P/P_0 \leqslant 1.0$), suggesting the coexistence of meso- (2–50 nm) and macropores (>50 nm). This can play the role of ion-buffering reservoirs, thus shortening the ion/mass transmission distance and facilitating the faradaic reactions at a high current density [12, 38, 45, 46]. The pore size distribution curves calculated by non-local density functional theory (NLDFT) are depicted in figure 2(g). All pore distribution curves show two major peaks at pore size ranges of 0.6–0.9 nm and 1–1.2 nm. An additional secondary wide peak ranging from 12 to 60 nm appears in the NLDFT pore distribution curves of HPCN-1, HPCN-2, HPCN-3 and HPCN-4, indicating that these four samples have well-developed hierarchical micro-, meso-, and macropore structures [12, 15, 16, 38, 39, 45, 47]. SSA values and pore volumes are summarized in table S3. The SSA values of HPCN-1, HPCN-2, HPCN-3, HPCN-4 and HPCN-5 are 876, 924, 1003, 989 and 1230 $m^2\ g^{-1}$, respectively, with corresponding t-plot micropore areas of 852, 888, 948, 955 and 1228 $m^2\ g^{-1}$. The external surface areas of HPCN-1, HPCN-2, HPCN-3, HPCN-4 and HPCN-5 calculated by the t-plot method are 23.66, 36.35, 55.18, 33.88 and 2.05 $m^2\ g^{-1}$, and their pore volumes are 0.41, 0.43, 0.47 0.81 and 0.47 $cm^3\ g^{-1}$, respectively. Notably, HPCN-5 has the largest micropore area and highest microporosity of 99.8%, which are a disadvantage for fast diffusion of electrolyte ions. As SP-5 has the largest particle size because of the lowest catalytic efficiency of acetic acid, the escape of heteroatoms is favorable for generating micropores instead of meso- and macropores during the carbonization process. From these results, we infer that the formation of coral reef-like structure in the Schiff base polymer precursors is beneficial for the generation of well-developed hierarchical pore structures in the carbon materials.

The XPS spectra of all carbon materials show three strong peaks of C, N, and O elements (figure 3(a)). Taking HPCN-3 as an example, the high-resolution C 1 s spectrum (figure 3(b)) is deconvolved into three signals, which are assigned to C=C/C–C (284.8 ± 0.1 eV), C–N/C–O (285.6 ± 0.1 eV) and C=O (288.2 ± 0.1 eV), respectively [48, 49]. The high-resolution N 1 s spectrum (figure 3(c)) is fitted to four peaks: pyridine N (N-6, 398.4 ± 0.1 eV), pyrrole N (N-5, 399.7 ± 0.1 eV), quaternary N (N-Q, 401.1 ± 0.1 eV) and oxidized-N (N-Ox, 403 ± 0.1 eV) [50, 51]. Normally, graphitic N can enhance conductivity, and pyridinic N and pyrrole N can create active sites, thus enhancing the electronic transmission and improving the generation of faradaic pseudo-capacitance [1, 9, 38, 44, 52]. In the case of the high-resolution O 1 s spectrum (figure 3(d)), two deconvoluted peaks centering at 531.5 ± 0.1 eV and 532.8 ± 0.1 eV are observed, ascribed to O=C and C–O–C/C–OH, respectively [53].

The element contents of C, N, and O evaluated from XPS measurements (figures 3 and S8) are provided in table S3, which reveal that HPCN-4 and HPCN-5 have lower N contents in comparison with that of HPCN-1, HPCN-2 and HPCN-3. This is possibly due to the fact that SP-4 and SP-5 have more protonated imine bonds and higher protonated amine content, derived from the excessive hydrogen ion concentration, which are the unstable species. Additionally, the catalytic activity of HAc is too low, making a large amount of unreacted amine group remains in SP-5, thus resulting in the loss of N atoms during carbonization process (table S3).

3.2. Electrochemical properties of HPCNs

To obtain the optimal carbonization temperature, SP-3 was carbonized at different temperatures, 750, 850 and 950 °C, to afford HPCN-6, HPCN-3 and HPCN-7, respectively. The electrochemical properties of these HPCNs were evaluated through CV and GCD measurements in a three-electrode system with the 1 M H_2SO_4 electrolyte at the potential

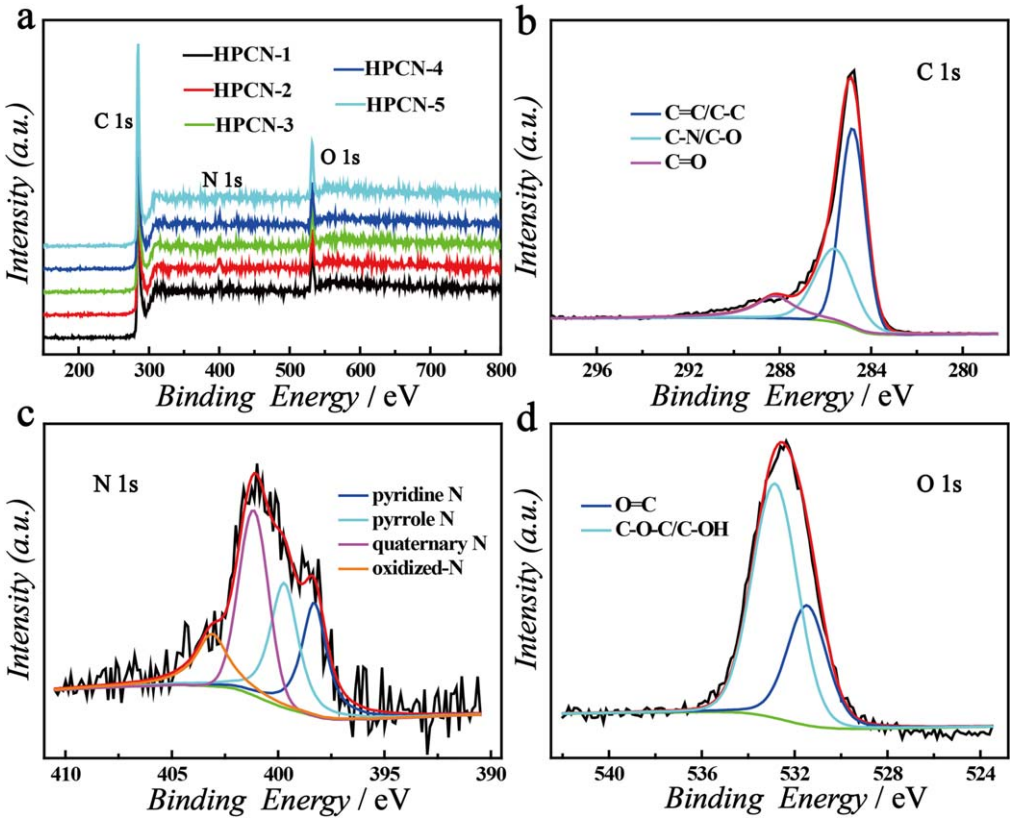

Figure 3. XPS spectra of all samples (a); high-resolution XPS spectra of HPCN-3: C 1s (b), N 1s (c) and O 1s (d).

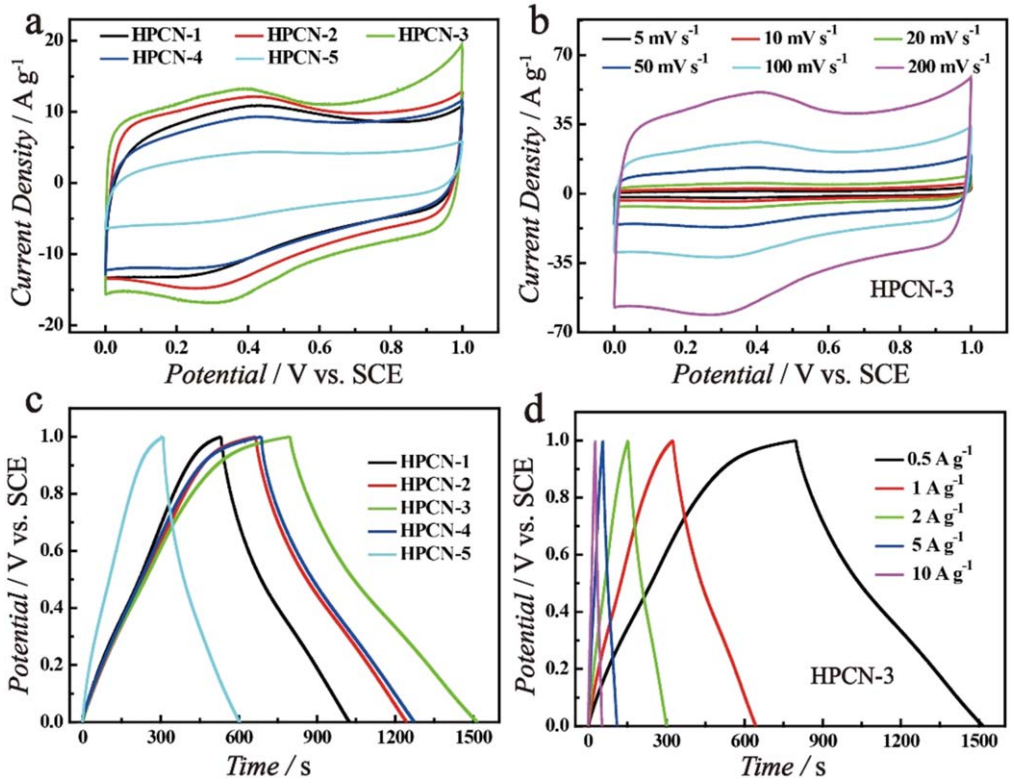

Figure 4. Electrochemical performance of HPCNs in 1 M H_2SO_4: CV curves of HPCNs at 50 mV s^{-1} (a); CV curves of HPCN-3 at scan rates from 5 to 200 mV s^{-1} (b); GCD profiles of HPCNs at 0.5 A g^{-1} (c); GCD profiles of HPCN-3 at current densities from 0.5 to 10 A g^{-1} (d).

window of 0–1 V. From the CV and GCD curves (figure S9), it is clear that HPCN-3 has the largest CV curve areas at a scan rate of 50 mV s^{-1}. Compared with HPCN-6 (242 F g^{-1}) and HPCN-7 (282.5 F g^{-1}), HPCN-3 also has a much higher specific capacitance (359.5 F g^{-1}) at the current density of 0.5 A g^{-1}. Therefore, we chose the carbonization temperature of 850 °C to generate other HPCNs.

The CV curves of the HPCNs at a scan rate of 50 mV s^{-1} (figure 4(a)) display similar quasi-rectangular shapes. Notably, the gradient of current density change at the switching potential of HPCN-3 approaches 90° and its CV area is larger in comparison with that of HPCN-1, HPCN-2, HPCN-4 and HPCN-5. Clearly, HPCN-3 shows much better electric double layer behavior and optimal supercapacitive performance [50, 54, 55]. With an increase in the scan rate from 5 to 200 mV s^{-1}, the current density distinctly increases, while the CV curves of HPCNs (figures 4(b), S10(a)–(d)) maintain the original quasi-rectangular shapes. Furthermore, broad redox peaks ranging from 0.1 to 0.5 V (versus Hg/Hg_2Cl_2) can be observed, which are associated with the redox reaction of the pyrrolic N, pyridinic N, and oxygen-containing functionalities [12, 53, 54, 56, 57]. GCD profiles of HPCNs at the current density of 0.5 A g^{-1} (figure 4(c)) display near isosceles triangular shapes and have no sharp IR drops during the discharging process, which manifests their good electrical conductivity and excellent electrochemical reversibility [14, 38]. Consistent with the CV results, the specific capacitance of HPCN-3 (359.5 F g^{-1}) is higher than that of HPCN-1 (246.5 F g^{-1}), HPCN-2 (290 F g^{-1}), HPCN-4 (289.5 F g^{-1}) and HPCN-5 (146.5 F g^{-1}) and is also superior or comparable to a previously reported work using the Schiff base formation reaction to make porous carbon materials (table S5).

Since redox peaks appear in CV curves and the shape of GCD profiles are deviated, the capacitance of HPCNs are composed of EDLC and faradaic capacitance. To evaluate the contributions of EDLC and faradaic capacitance to the total capacitance, equation (1) is employed and the specific form is given as follow [38, 58, 59]:

$$C = k_1 + k_2 t^{1/2}, \quad (1)$$

where k_1 corresponds to the rate independent part associated with EDLC, $k_2 t^{1/2}$ represents the limited diffusion portion depending on the current density, and t is discharge time. The trends of the capacitance values with the square root of the discharge time are depicted in figures S11(a)–(e). Based on the theory of equation (1), the value of the intersection point of the dotted line and the Y-axis is consistent with the contribution of EDLC, and the detailed results are summarized in table S4. At a current density of 0.5 A g^{-1}, the capacitances rooted in EDLC of HPCN-1, HPCN-2, HPCN-3, HPCN-4 and HPCN-5 are 190, 210, 240, 186 and 70 F g^{-1}, with corresponding faradaic capacitance portions of 56.5, 80, 119.5, 103, and 76.5 F g^{-1}, respectively. Theoretically, carbon materials with large SSAs have outstanding EDLC, and while this possesses high heteroatom content, excellent faradaic capacitance can be expected. Intriguingly, HPCN-3 displays optimal EDLC and faradaic capacitance, but shows medium SSA and heteroatom content, as identified by N_2 adsorption–desorption measurements and XPS. This result may be related to the different utilizations of SSA and heteroatoms due to the difference in SSA and morphologies. To give a deep insight into the reason, the EDLC is normalized by the SSA and the faradaic capacitance is normalized by the heteroatom content [21, 60]. As presented in table S4, HPCN-1, HPCN-2, HPCN-3, HPCN-4, and HPCN-5 have normalized EDLC values of 0.216, 0.227, 0.239, 0.188, and 0.056 F m^{-2}, and normalized faradaic capacitances of 4.98, 7.24, 10.24, 9.12, and 5.93 F g^{-1}, respectively. Clearly, HPCN-3 with secondary SSA shows the largest normalized EDLC, while HPCN-5, possessing the largest SSA, displays the smallest normalized EDLC. Probably, the coral reef-like morphology is favorable towards exposing a greater external surface area, which makes the SSA easy to be exploited, whereas the larger particle size of HPCN-5 is disadvantageous for the electrolyte ion penetrating into the bulk body of carbon materials, resulting in the poor use of micropores. In addition, HPCN-3 shows superior normalized faradaic capacitance, which can be explained by two factors: (i) the coral reef-like morphology is likely to expose more heteroatoms on the external surface area, and thereby the electrolyte ion is easier to access heteroatoms on the surface; (ii) the larger SSA improves the electroadsorbed possibilities between the electrolyte ion and heteroatoms. Hence, the SSA and morphology of electrode materials have a significant effect on the efficient utilization of SSA and heteroatoms, therefore leading to enhanced capacitance.

To measure the rate capability of HPCNs electrodes, GCD profiles at different current densities (0.5 to 30 A g^{-1}) were tested (figures 4(d), S10(e)–(h) and S12). Specifically, even at a high current density of 30 A g^{-1}, the specific capacitances of HPCN-1, HPCN-2, HPCN-3, HPCN-4 and HPCN-5 remain 156.6, 194.7, 236.4, 135.3 and 47 F g^{-1}, respectively. In reference to the capacitances at a current density of 0.5 A g^{-1}, the rate retention performance of these samples are 63.53%, 67%, 65.8%, 46.73% and 32.08%, respectively (figure 5(a)). This trend implies that the coral reef-like structure can facilitate the fast transport of electrolyte ions at high current densities, thereby improving the rate performance of the electrode materials [61, 62].

To obtain a deep understanding of the intrinsic electrochemical behavior of as-prepared carbon materials, EIS was performed (figures 5(b), (c)). From the Nyquist plot, HPCN-3 shows the steepest line near 90° at the low-frequency range, indicating its remarkable electrical double layer capacitance behavior. The solution resistance (Rs) and charge-transfer resistance (Rct) between the electrode and electrolyte were calculated based on the equivalent circuit shown in figure 5(b). Also, the Rs values of HPCN-1, HPCN-2, HPCN-3, HPCN-4 and HPCN-5 are 0.56, 0.51, 0.49, 0.56, and 0.65 Ω, and the corresponding Rct values are 0.75, 0.71, 0.74, 0.8 and 1.09 Ω, respectively. Clearly, the Rs and Rct values of HPCN-5 are significantly higher than the others, suggesting that the bulk structures are not conducive to mass/charge transmission. HPCN-3 exhibits both relatively small Rs and Rct values, demonstrating its superior electron conduction and faster ion/charge diffusion ability in the electrolyte [63].

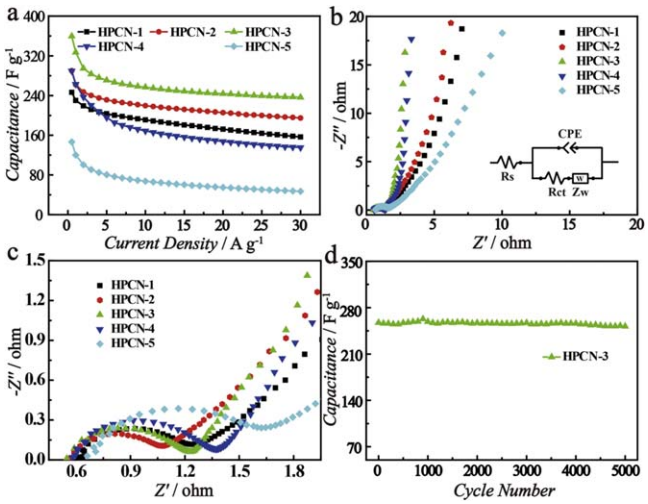

Figure 5. Specific capacitance as a function of different current densities of HPCNs (a); the Nyquist plots (b) and the magnified higher-frequency region of the Nyquist plots (c)of HPCNs; the stability evaluation of HPCN-3 at 10 A g^{-1} (d).

These results further demonstrate that HPCN-3 possesses the best capacitive behavior.

The cycle life of electrode materials is also a major parameter affecting the practical application of supercapacitors [2]. Thus, the cycle stability of HPCN-3, which showed the best capacitance performance, was characterized by GCD cycling at a current density of 10 A g^{-1} for 5000 times. The capacitance retention of HPCN-3 electrodes eventually reached up to 97.9%, confirming the outstanding cycle stability as well as its reasonable morphology and pore structure (figure 5(d)).

3.3. Electrochemical performance of semi-solid-state symmetrical supercapacitor

We also evaluated the electrochemical performance of HPCN-3 in a semi-solid-state symmetrical supercapacitor. As shown in figure 6(a), all CV curves can retain a similar rectangular shape at scan rates varying from 5 to 200 mV s^{-1}. The GCD profiles of the as-prepared supercapacitor depicted in figure 6(b) demonstrate a triangle-like shape at current density ranging from 0.5 to 10 A g^{-1}. The specific capacitance of the semi-solid-state supercapacitor is 55 F g^{-1} at a current density of 0.5 A g^{-1}, and the corresponding capacitance of the single HPCN-3 electrode is 220 F g^{-1}. To evaluate the rate performance of the supercapacitor, GCD measurements at different current densities were tested. The capacitance remains at 130.5 F g^{-1} at a current density of 20 A g^{-1}, and thus good rate performance (59.3%) can be achieved from 0.5 to 20 A g^{-1} (figure 6(c)). Figure 6(d) shows the Ragone plot calculated through the GCD data at varying current densities: the energy density of the as-prepared supercapacitor decreases from 7.64 to 4.86 Wh kg^{-1}, while the power density increases from 0.25 to 5 kW kg^{-1}. This result implies that the energy density of our HPCN-3 based semi-solid-state symmetrical supercapacitor is below the medium level of the reported supercapacitor devices with doped carbon materials as the electrodes and PVA/H_2SO_4 gel as the electrolyte [64–67]. Notably, one supercapacitor device can light up a small LED bulb (the inset picture in

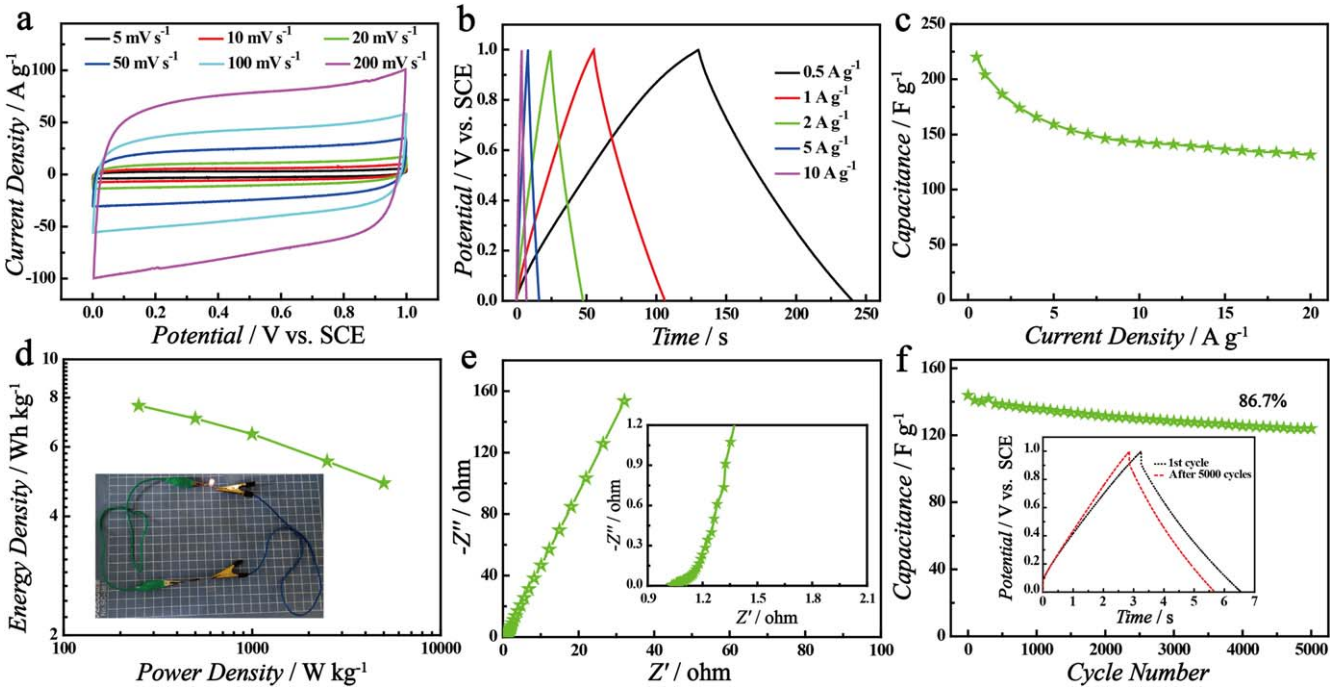

Figure 6. Electrochemical performance of HPCN-3 in a semi-solid-state supercapacitor: CV curves at a scan rate varying from 5 to 200 mV s^{-1} (a); GCD profiles at current densities from 0.5 to 10 A g^{-1} (b); specific capacitance as a function of different current densities (c); the Ragone plot calculated through GCD data at varying current densities and the picture of using as-prepared supercapacitor to light up an LED bulb (d); the Nyquist plots, with the inset showing the magnified higher-frequency region (e); the cycle stability at the current density of 10 A g^{-1}, with the inset showing the comparison of the first and last lap of GCD profiles (f).

figure 6(d)). EIS measurement was used to demonstrate the ion diffusion and charge transfer ability (figure 6(e)). The Nyquist plot shows an inconspicuous small semi-circular arc in the high-frequency region, suggesting excellent charge transfer ability between the electrode and electrolyte [38, 68, 69]. The linear part of the low-frequency region symbolizes the ideal capacitive behavior of this device. Moreover, we evaluated the cycle ability of the as-prepared device through the GCD cycles. After 5000 cycles of charge and discharge processes at a current density of 10 A g^{-1}, as displayed in figure 6(f), the capacitance retention rate was 86.7%, exhibiting good electrochemical reversibility of electrodes.

4. Conclusion

In summary, through a simple Schiff base formation reaction, a series of SPs with different morphologies were successfully synthesized by adjusting the concentration of catalyst TfOH, or replacing TfOH with SA and HAc. This was followed by a simple one-step carbonization procedure where N/O co-doped hierarchical porous HPCNs possessing different morphologies, SSAs and pore structures were prepared. The HPCNs exhibited excellent electrochemical performance in the 1 M H_2SO_4 electrolyte. The coral reef-like HPCN-3 has a high SSA of 1003 m^2 g^{-1}, a hierarchical porous structure, and the highest specific capacitance of 359.5 F g^{-1} at a current density of 0.5 A g^{-1}. Additionally, a semi-solid-state symmetrical supercapacitor based on HPCN-3 electrodes was constructed, the as-prepared device exhibited a capacitance of 55 F g^{-1} at 0.5 A g^{-1}, and the energy density was 7.64 Wh kg^{-1} (4.86 Wh kg^{-1}) while the power density was 0.25 kW kg^{-1} (5 kW kg^{-1}). This research demonstrates that changing the species or concentration of the catalyst during the synthesis of Schiff base polymer precursors can cause a difference in morphology and in the composition of polymers, ultimately affecting the electrochemical performance of the carbon materials, which is instructive for the development of heteroatom-doped carbon materials; simultaneously, increasing the external surface area can improve the effective utilization of the SSA and heteroatoms, which has important guiding significance for the design of electrode materials in supercapacitors.

Acknowledgments

This work was supported by the National Natural Science Foundation of China (51673161, 51773172, U1805253); Natural Science Foundation of Fujian Province (2019J01032); Scientific and Technological Innovation Platform of Fujian Province (2014H2016); and Science and Technology Major Project of the Fujian Province (2018HZ0001-1).

Data availability statement

All data that support the findings of this study are included within the article (and any supplementary files).

ORCID iDs

Yiting Xu https://orcid.org/0000-0001-7729-8616
Conghui Yuan https://orcid.org/0000-0003-0126-7236

References

[1] Hao L, Li X L and Zhi L J 2013 Carbonaceous electrode materials for supercapacitors *Adv. Mater.* **25** 3899–904
[2] Raza W, Ali F Z, Raza N, Luo Y W, Kim K H, Yang J H, Kumar S, Mehmood A and Kwon E E 2018 Recent advancements in supercapacitor technology *Nano Energy* **52** 441–73
[3] Yu Z N, Tetard L, Zhai L and Thomas J 2015 Supercapacitor electrode materials: nanostructures from 0 to 3 dimensions *Energy Environ. Sci.* **8** 702–30
[4] Geng P B, Zheng S S, Tang H, Zhu R M, Zhang L, Cao S, Xue H G and Pang H 2018 Transition metal sulfides based on graphene for electrochemical energy storage *Adv. Energy Mater.* **8** 1703259
[5] Salunkhe R R, Kaneti Y V and Yamauchi Y 2017 Metal-organic framework-derived nanoporous metal oxides toward supercapacitor applications: progress and prospects *ACS Nano* **11** 5293–308
[6] Augustyn V, Simon P and Dunn B 2014 Pseudocapacitive oxide materials for high-rate electrochemical energy storage *Energy Environ. Sci.* **7** 1597–614
[7] Meng Q F, Cai K F, Chen Y X and Chen L D 2017 Research progress on conducting polymer based supercapacitor electrode materials *Nano Energy* **36** 268–85
[8] Baker C O, Huang X W, Nelson W and Kaner R B 2017 Polyaniline nanofibers: broadening applications for conducting polymers *Chem. Soc. Rev.* **46** 1510–25
[9] Liu D B, Ni K, Ye J L, Xie J, Zhu Y W and Song L 2018 Tailoring the structure of carbon nanomaterials toward high-end energy applications *Adv. Mater.* **30** 1802104
[10] Liu L L, Niu Z Q and Chen J 2016 Unconventional supercapacitors from nanocarbon-based electrode materials to device configurations *Chem. Soc. Rev.* **45** 4340–63
[11] Zhu D Z, Jiang J X, Sun D M, Qian X Y, Wang Y W, Li L C, Wang Z W, Chai X L, Gan L H and Liu M X 2018 A general strategy to synthesize high-level N-doped porous carbons via Schiff-base chemistry for supercapacitors *J. Mater. Chem.* A **6** 12334–43
[12] Li Y T, Liu L, Wu Y Z, Wu T, Wu H Y, Cai Q P, Xu Y T, Zeng B R, Yuan C H and Dai L Z 2019 Facile synthesis of nitrogen-doped carbon materials with hierarchical porous structures for high-performance supercapacitors in both acidic and alkaline electrolytes *J. Mater. Chem.* A **7** 13154–63
[13] Lin Z C and Qiao X W 2018 Coral-like Co_3O_4 decorated N-doped carbon particles as active materials for oxygen reduction reaction and supercapacitor *Sci. Rep.* **8** 1802
[14] Li Y J, Zheng S H, Liu X, Li P, Sun L, Yang R X, Wang S, Wu Z S, Bao X H and Deng W Q 2018 Conductive microporous covalent triazine-based framework for high-performance electrochemical capacitive energy storage *Angew. Chem.* **130** 8124–8

[15] Li J, Wang N, Tian J R, Qian W Z and Chu W 2018 Cross-coupled macro-mesoporous carbon network toward record high energy-power density supercapacitor at 4 V *Adv. Funct. Mater.* **28** 1806153

[16] Yang W, Yang W, Kong L N, Song A L, Qin X J and Shao G J 2018 Phosphorus-doped 3D hierarchical porous carbon for high-performance supercapacitors: a balanced strategy for pore structure and chemical composition *Carbon* **127** 557–67

[17] Chen W, Rakhi R B, Wang Q X, Hedhili M N and Alshareef H N 2014 Morphological and electrochemical cycling effects in MnO_2 nanostructures by 3D electron tomography *Adv. Funct. Mater.* **24** 3130–43

[18] Ramachandran R, Zhao C H, Luo D, Wang K and Wang F 2018 Morphology-dependent electrochemical properties of cobalt-based metal organic frameworks for supercapacitor electrode materials *Electrochim. Acta* **267** 170–80

[19] Jian X, Liu S Y, Gao Y Q, Zhang W L, He W D, Mahmood A, Subramaniyam C M, Wang X L, Mahmood N and Dou S X 2017 Facile synthesis of three-dimensional sandwiched MnO_2@GCs@MnO_2 hybrid nanostructured electrode for electrochemical capacitors *ACS Appl. Mater. Interfaces* **9** 18872–82

[20] Guan B Y, Yu X Y, Wu H B and Lou X W 2017 Complex nanostructures from materials based on metal-organic frameworks for electrochemical energy storage and conversion *Adv. Mater.* **29** 1703614

[21] Chang Y, Yuan C H, Liu C, Mao J, Li Y T, Wu H Y, Wu Y Z, Xu Y T, Zeng B R and Dai L Z 2017 B, N co-doped carbon from cross-linking induced self-organization of boronate polymer for supercapacitor and oxygen reduction reaction *J. Power Sources* **365** 354–61

[22] Miao L, Duan H, Zhu D Z, Lv Y K, Gan L H, Li L C and Liu M X 2021 Boron 'gluing' nitrogen heteroatoms in a prepolymerized ionic liquid-based carbon scaffold for durable supercapacitive activity *J. Mater. Chem.* A **9** 2714–24

[23] Li H, Bai J, Shi Z X and Yin J 2016 Environmental friendly polymers based on Schiff-base reaction with self-healing, remolding and degradable ability *Polymer* **8** 106–13

[24] Ou H J, You Q L, Li J, Liao G Y, Xia H and Wang D S 2016 A rich-amine porous organic polymer: an efficient and recyclable adsorbent for removal of azo dye and chlorophenol *RSC Adv.* **6** 98487–97

[25] Yan J J, Miao L, Duan H, Zhu D Z, Lv Y K, Xiong W, Li L C, Gan L H and Liu M X 2020 core–shell hierarchical porous carbon spheres with N/O doping for efficient energy storage *Electrochim. Acta* **358** 136899

[26] Mansuer M, Miao L, Zhu D Z, Duan H, Lv Y K, Li L C, Liu M X and Gan L H 2021 Facile construction of highly redox active carbons with regular micropores and rod-like morphology towards high-energy supercapacitors *Mater. Chem. Front.* **5** 3061–72

[27] Xu X B, Lu S Y, Gao C M, Wang X G, Bai X, Duan H G, Gao N N, Feng C and Liu M Z 2015 Polymeric micelle-coated mesoporous silica nanoparticle for enhanced fluorescent imaging and pH-responsive drug delivery *Chem. Eng. J.* **279** 851–60

[28] Wan Y M, Bu Y, Liu J M, Yang J, Cai W Q, Yin Y H, Xu W J, Xu P H, Zhang J L and He M 2018 pH and reduction-activated polymeric prodrug nanoparticles based on a 6-thioguanine-dialdehyde sodium alginate conjugate for enhanced intracellular drug release in leukemia *Polym. Chem.* **9** 3415–24

[29] Dai T J, Wang C P, Wang Y Q, Xu W, Hu J J and Cheng Y Y 2018 A nanocomposite hydrogel with potent and broad-spectrum antibacterial activity *ACS Appl. Mater. Interfaces* **10** 15163–73

[30] Liu S L, Kang M M, Li K W, Yao F, Oderinde O, Fu G D and Xu L Q 2018 Polysaccharide-templated preparation of mechanically-tough, conductive and self-healing hydrogels *Chem. Eng. J.* **334** 2222–30

[31] Wei H T, Ning J, Cao X D, Li X H and Hao L 2018 Benzotrithiophene-based covalent organic frameworks: construction and structure transformation under ionothermal condition *J. Am. Chem. Soc.* **140** 11618–22

[32] Segura J L, Mancheno M J and Zamora F 2016 Covalent organic frameworks based on Schiff-base chemistry: synthesis, properties and potential applications *Chem. Soc. Rev.* **45** 5635–71

[33] Yang W D, Liu C Y, Zhang Z Y, Liu Y and Nie S D 2012 One step synthesis of uniform organic silver ink drawing directly on paper substrates *J. Mater. Chem.* **22** 23012–6

[34] Stevens J S, Byard S J, Seaton C C, Sadiq G, Davey R J and Schroeder S L M 2014 Proton transfer and hydrogen bonding in the organic solid state: a combined XRD/XPS/ssNMR study of 17 organic acid-base complexes *Phys. Chem. Chem. Phys.* **16** 1150–60

[35] Stevens J S, Byard S J, Seaton C C, Sadiq G, Davey R J and Schroeder S L M 2011 Crystallography aided by atomic core-level binding energies: proton transfer versus hydrogen bonding in organic crystal structures *Angew. Chem. Int. Ed.* **50** 9916–8

[36] Ding X, Xiao D, Ji L, Jin D, Dai K, Yang Z X, Wang S Y and Chen H 2018 Simple fabrication of Fe_3O_4/C/g-C_3N_4 two-dimensional composite by hydrothermal carbonization approach with enhanced photocatalytic performance under visible light *Catal. Sci. Technol.* **8** 3484–92

[37] Matsumoto M, Dasari R, Ji W, Feriante C, Parker T, Marder S and Dichtel W 2017 Rapid, low temperature formation of imine-linked covalent organic frameworks catalyzed by metal triflates *J. Am. Chem. Soc.* **139** 4999–5002

[38] Song Z Y, Zhu D Z, Li L C, Chen T, Duan H, Wang Z W, Lv Y K, Xiong W, Liu M X and Gan L H 2019 Ultrahigh energy density of a N, O co-doped carbon nanosphere based all-solid-state symmetric supercapacitor *J. Mater. Chem.* A **7** 1177–86

[39] Dutta S, Bhaumik A and Wu K C W 2014 Hierarchically porous carbon derived from polymers and biomass: effect of interconnected pores on energy applications *Energy Environ. Sci.* **7** 3574–92

[40] Urbonaite S, Halldahl L and Svensson G 2008 Raman spectroscopy studies of carbide derived carbons *Carbon* **46** 1942–7

[41] Osswald S, Flahaut E and Gogotsi Y 2006 *In situ* Raman spectroscopy study of oxidation of double-and single-wall carbon nanotubes *Chem. Mater.* **18** 1525–33

[42] Yang J, Xu M, Wang J Y, Jin S B and Tan B E 2018 A facile approach to prepare multiple heteroatom-doped carbon materials from imine-linked porous organic polymers *Sci. Rep.* **8** 4200

[43] Song B, Sizemore C, Li L Y, Huang X G, Lin Z Y, moon K S and Wong C P 2015 Triethanolamine functionalized graphene-based composites for high performance supercapacitors *J. Mater. Chem.* A **3** 21789–96

[44] Ouyang T, Cheng K, Gao Y Y, Kong S Y, Ye K, Wang G L and Cao D X 2016 Molten salt synthesis of nitrogen doped porous carbon: a new preparation methodology for high-volumetric capacitance electrode materials *J. Mater. Chem.* A **4** 9832–43

[45] Deshmukh A B, Nalawade A C, Karbhal I, Qureshi M S and Shelke M V 2018 Electrochemical capacitive energy storage in PolyHIPE derived nitrogen enriched hierarchical porous carbon nanosheets *Carbon* **128** 287–95

[46] Wang J G, Liu H Z, Zhang X Y, Shao M H and Wei B Q 2018 Elaborate construction of N/S-co-doped carbon nanobowls

for ultrahigh-power supercapacitors *J. Mater. Chem.* A **6** 17653–61

[47] Zhao J, Jiang Y F, Fan H, Liu M, Zhuo O, Wang X Z, Wu Q, Yang L J, Ma Y W and Hu Z 2017 Porous 3D few-layer graphene-like carbon for ultrahigh-power supercapacitors with well-defined structure-performance relationship *Adv. Mater.* **29** 1604569

[48] Wu X Y, Ma C H, Liu J C, Liu Y S, Luo S, Xu M C, Wu P, Li W and Liu S X 2019 In-situ green synthesis of nitrogen-doped carbon dots-based room temperature phosphorescence materials for visual iron ion detection *ACS Sustainable Chem Eng* **7** 18801–9

[49] Pang Y P, Wang J, Yang J H, Fang F, Sun D L and Zheng S Y 2019 Fully reversible lithium storage of tin oxide enabled by self-doping and partial amorphization *Nanoscale* **11** 12915–23

[50] Chen Z, Ye S J, Evans S D, Ge Y H, Zhu Z F, Tu Y F and Yang X M 2018 Confined assembly of hollow carbon spheres in carbonaceous nanotube: a spheres-in-tube carbon nanostructure with hierarchical porosity for high-performance supercapacitor *Small* **14** 1704015

[51] Hao L *et al* 2012 Terephthalonitrile-derived nitrogen-rich networks for high performance supercapacitors *Energy Environ. Sci.* **5** 9747–51

[52] Yang M and Zhou Z 2017 Recent breakthroughs in supercapacitors boosted by nitrogen-rich porous carbon materials *Adv. Sci.* **4** 1600408

[53] Zhou M, Li X Y, Zhao H, Wang J, Zhao Y P, Ge F Y and Cai Z S 2018 Combined effect of nitrogen and oxygen heteroatoms and micropores of porous carbon frameworks from Schiff-base networks on their high supercapacitance *J. Mater. Chem.* A **6** 1621–9

[54] Qin F F, Tian X D, Guo Z Y and Shen W Z 2018 Asphaltene-based porous carbon nanosheet as electrode for supercapacitor *ACS Sustainable Chem Eng* **6** 15708–19

[55] Jiang H, Lee P S and Li C Z 2013 3D carbon based nanostructures for advanced supercapacitors *Energy Environ. Sci.* **6** 41–53

[56] Tang C G, Liu Y J, Yang D G, Yang M and Li H M 2017 Oxygen and nitrogen co-doped porous carbons with finely-layered schistose structure for high-rate-performance supercapacitors *Carbon* **122** 538–46

[57] Zhang R, Jing X X, Chu Y T, Wang L, Kang W J, Wei D H, Li H B and Xiong S L 2018 Nitrogen/oxygen co-doped monolithic carbon electrodes derived from melamine foam for high-performance supercapacitors *J. Mater. Chem.* A **6** 17730–9

[58] Lin T Q, Chen I W, Liu F X, Yang C Y, Bi H, Xu F F and Huang F Q 2015 Nitrogen-doped mesoporous carbon of extraordinary capacitance for electrochemical energy storage *Science* **350** 1508–13

[59] Wang Q, Qin B, Zhang X H, Xie X L, Jin L E and Cao Q 2018 Synthesis of N-doped carbon nanosheets with controllable porosity derived from bio-oil for high-performance supercapacitors *J. Mater. Chem.* A **6** 19653–63

[60] Sheberla D, Bachman J C, Elias J S, Sun C J, Shao-Horn Y and Dinca M 2017 Conductive MOF electrodes for stable supercapacitors with high areal capacitance *Nat. Mater.* **16** 220–4

[61] Wang S, Zhang L, Han F, Li W C, Xu Y Y, Qu W H and Lu A H 2014 Diaminohexane-assisted preparation of coral-like, poly (benzoxazine)-based porous carbons for electrochemical energy storage *ACS Appl. Mater. Interfaces* **6** 11101–9

[62] Liu Y J, Hu X, Zhong G B, Chen J X, Zhan H B and Wen Z H 2019 Layer-by-layer stacked nanohybrids of N, S-co-doped carbon film modified atomic MoS_2 nanosheets for advanced sodium dual-ion batteries *J. Mater. Chem.* A **7** 24271–80

[63] Li Z Y, Fan X N, Wang R F, Yang Q B, Guo M L, Wu Y P, Wang J F and Chen J Y 2020 Activation-free, porous and superamphiphilic N-doped carbon capsular nanofibrous electrode for high performance electrochemical capacitor *J. Power Sources* **463** 228112

[64] Anothumakkool B, Torris A T A, Bhange S, Badigerb M and Kurungot S 2014 Electrodeposited polyethylenedioxythiophene with infiltrated gel electrolyte interface: a close contest of an all-solid-state supercapacitor with its liquid-state counterpart *Nanoscale* **6** 5944–52

[65] Meng C Z, Liu C H, Chen L Z, Hu C H and Fan S S 2010 Highly flexible and all-solid-state paperlike polymer supercapacitors *Nano Lett.* **10** 4025–31

[66] Zhao Y H, Liu P, Zhuang X D, Wu D Q, Zhang F and Su Y Z 2017 Ionothermally synthesized hierarchical porous Schiff-base-type polymeric networks with ultrahigh specific surface area for supercapacitors *RSC Adv.* **7** 19934–9

[67] Cao A P, Li Y F, Chen Z X, Wang Y M, Li T X and Han Y Q 2020 Polymerization of polypyrrole nanospheres on carbon nanotubes with $PMo_{12-x}W_x$ as oxidant and redox dopant for supercapacitor *Polymer* **204** 122829

[68] Wang Y, Wang S B and Lou X W 2019 Dispersed nickel cobalt oxyphosphide nanoparticles confined in multichannel hollow carbon fibers for photocatalytic CO_2 reduction *Angew Chem. In. Ed.* **58** 17236–40

[69] Liu Z W *et al* 2018 Zero-strain $K_{0.6}Mn_1F_{2.7}$ hollow nanocubes for ultrastable potassium ion storage *Energy Environ. Sci.* **11** 3033–42